Universiteit
Leiden
The Netherlands

On shape and elasticity: bio-sheets, curved crystals, and odd droplets

Garcia Aguilar, I.R.

Citation
Garcia Aguilar, I. R. (2022, September 13). *On shape and elasticity: bio-sheets, curved crystals, and odd droplets*. *Casimir PhD Series*. Retrieved from https://hdl.handle.net/1887/3458390

Version:	Publisher's Version
License:	Licence agreement concerning inclusion of doctoral thesis in the Institutional Repository of the University of Leiden
Downloaded from:	https://hdl.handle.net/1887/3458390

Note: To cite this publication please use the final published version (if applicable).

Chapter 4

Faceting and flattening of emulsion droplets

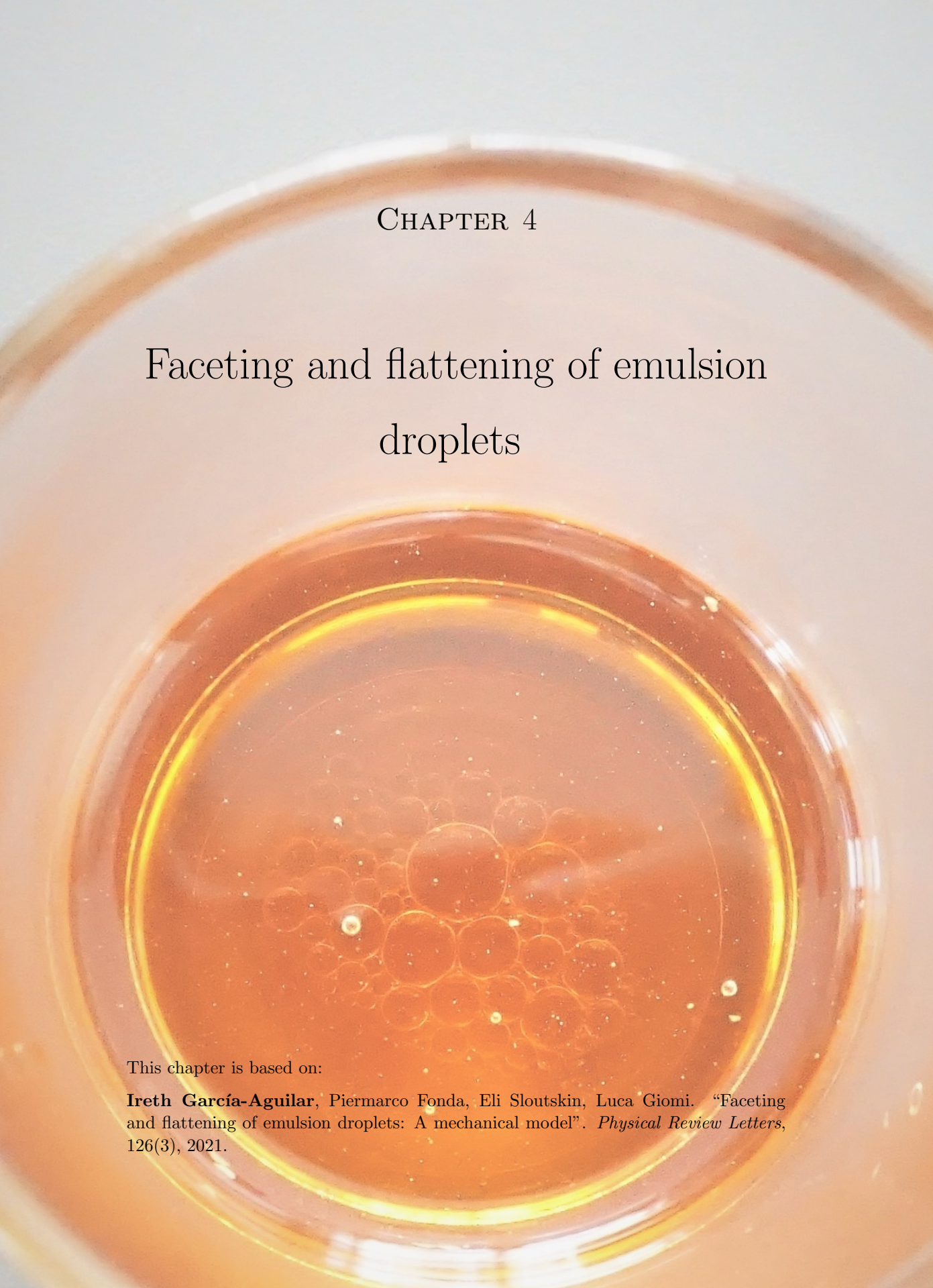

This chapter is based on:

Ireth García-Aguilar, Piermarco Fonda, Eli Sloutskin, Luca Giomi. "Faceting and flattening of emulsion droplets: A mechanical model". *Physical Review Letters*, 126(3), 2021.

When cooled down, emulsion droplets stabilized by a frozen interface of alkane molecules and surfactants have been observed to undergo a spectacular sequence of morphological transformations: from spheres to faceted liquid icosahedra, down to flattened liquid platelets. While generally ascribed to the interplay between the elasticity of the frozen interface and surface tension, the physical mechanisms underpinning these transitions have remained elusive, despite different theoretical pictures having been proposed in recent years. In this chapter, we introduce a comprehensive mechanical model of morphing emulsion droplets, which quantitatively accounts for various experimental observations, including the size scaling behavior of the faceting transition. Our analysis highlights the role of gravity and the spontaneous curvature of the frozen interface in determining the specific transition pathway.

4.1 Introduction: Deforming emulsion droplets

Despite liquid drops representing the quintessential realization of spherical geometry across an extraordinary vast range of length scales, from stars down to micro and nanoscale aerosols, a variety of faceted polyhedral shapes has been reported in simple oil-in-water emulsions [53] and recently investigated by Denkov *et al.* [37] and Guttman *et al.* [38] (Fig. 4.1 and Fig. 4.2. Unlike typical emulsion droplets, these are enclosed by an interfacially-frozen monolayer of mixed alkane molecules and surfactants (see Fig. 4.1b). Upon cooling below the freezing temperature of the interface, the droplets undergo a series of shape transformations: from spheres to icosahedra, to hexagonal platelets (Fig. 4.1a), to even more exotic shapes featuring tentacle-like protrusions [38]. The specific transition pathway is not universal, but depends on several factors, such as the oil and surfactant chemical composition, the cooling rate and the droplet size [37, 38, 90–92].

Whereas these fascinating experimental results are now reproducible (see Ref. [93] for a recent overview), a convincing explanation of the physical mechanisms underpinning the sequence of shape transformations is still lacking, despite two alternative scenarios having been proposed [37, 38, 84, 85, 90–92, 94–96]. The first, hereafter referred to as rotator phase mechanism [37, 94], revolves around the existence of a rotator phase in the proximity of the droplet's surface, whose estimated thickness ranges between 45 [96] and 300 nm [37], serving as a plastic scaffold for the observed shape transformations, especially across different flat morphologies [94]. The second scenario, proposed in Refs. [38, 85] and referred to as elastic buckling mechanism, ascribes instead the transformations to a competition between the stretching elasticity of the frozen interfacial monolayer and surface tension. As the former consists of a triangular lattice [97] lying on a closed surface, its structure is geometrically frustrated and inevitably features topological defects, where the local sixfold rotational symmetry of the lattice is broken [39] (see for example Fig. 4.1c). Furthermore, since the elastic stress introduced by these defects can be relieved by increasing the local

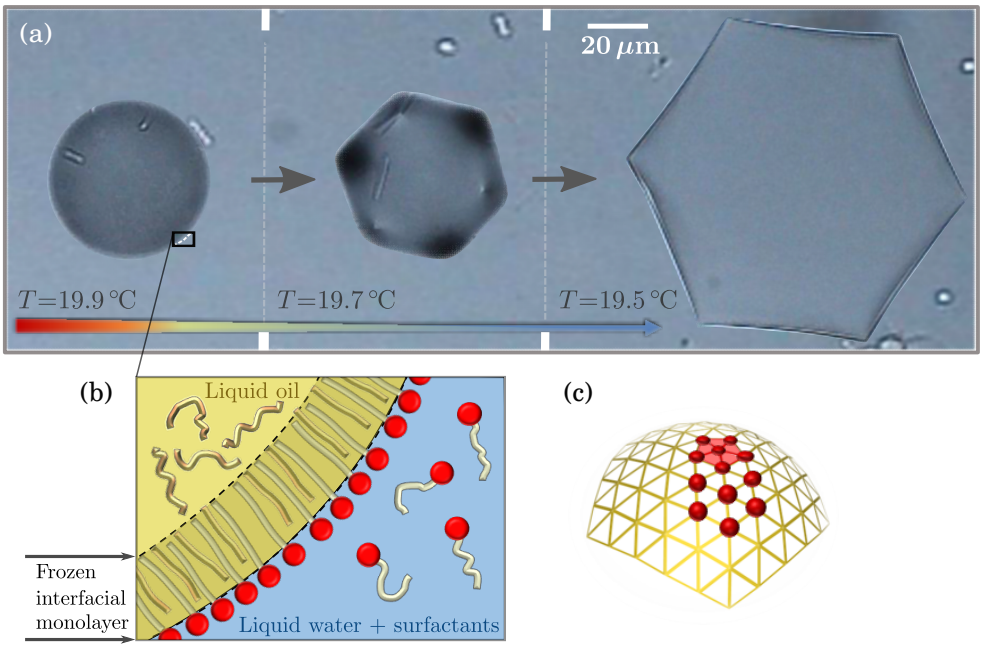

Figure 4.1: Deforming emulsion droplets (a) Light microscopy snapshots of the volume-conserving faceting and flattening of a single spherical droplet as temperature is lowered. (b) A schematic of the frozen interface of the droplets shows a monolayer of mixed alkane molecules and surfactants (with red heads) based on Ref. [38]. Below its freezing temperature the interface crystallizes, while the bulk water and oil remain liquid, leading the extended molecules to pack into a triangular lattice when viewed along the surface normal, as illustrated in (c). The closed crystalline interface is forced to accommodate topological disclinations, such as the one marked with a red pentagon, which introduce deforming stresses.

curvature[1] [52, 72], such a crystalline monolayer is generally prone to buckling and faceting. The most prominent example of this mechanism is found in the context of viral capsids. In these, the trade-off between in-plane stresses, originating from the presence of twelve topologically required fivefold disclinations, and bending moments, resulting from out-of-plane deformations, drives the buckling of spheres into icosahedra [49, 75, 82]. The transition occurs at large values of the so called Föppl-von Kármán number, YR^2/k, expressing the ratio between the stretching and bending energy scale, with Y the two-dimensional Young modulus, R the system size (e.g. the capsid radius prior to buckling) and k the bending rigidity. Thus, large viral capsids are energetically favored to be icosahedral, while small capsids are preferentially spherical.

Although potentially plausible to justify the observed sequence of shape transformations, neither of these scenarios succeeds in explaining all the experimental observations. Recent cryo-transmission electron (CryoTEM) micrographs revealed that the

[1] As also discussed more in detail in our work in Chapter 3.

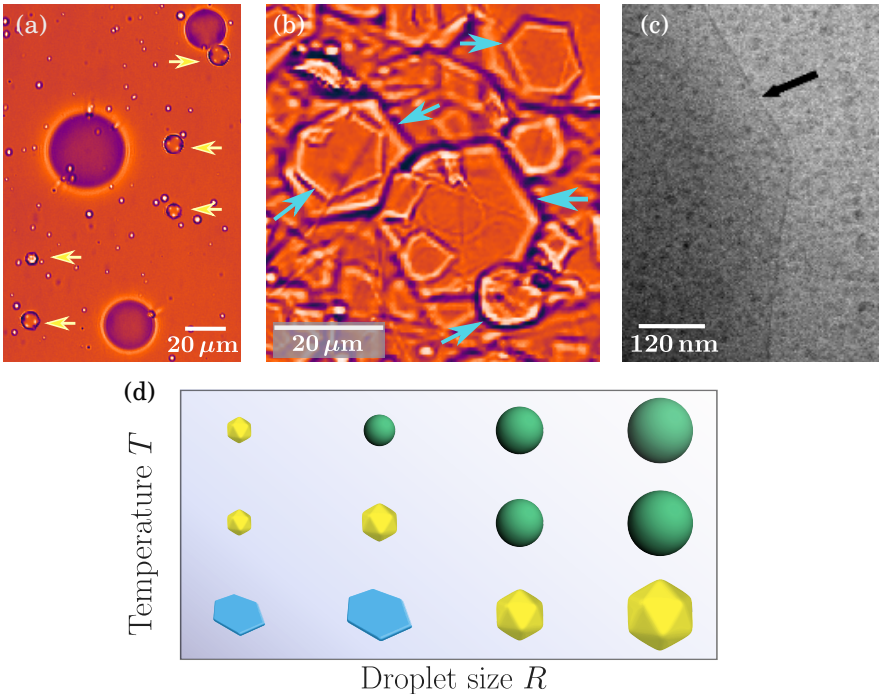

Figure 4.2: Experimental insights in the shape transformations. (a) Typical configuration of a polydispersed sample showing large spherical and small icosahedral droplets (highlighted by arrows). (b) Icosahedral droplets and platelets are oriented with a flat face orthogonal to the direction of gravity. (c) CryoTEM image of the interface of an icosahedral droplet, revealing that the thickness of the crystalline structure is close to 3 nm, corresponding solely to the interfacially-frozen monolayer. Reprinted and adapted with permission from [84]. Copyright (2019) American Chemical Society. (d) Schematic of the phase diagram of the droplets based on the experimental observations, with the triangulated surfaces used in the numerical calculations of the energy (see Eq. (4.3)).

solid layer located at the oil-water interface of small icosahedral and other polyhedral droplets is only a few nanometers thick (Fig. 4.2c and Refs. [84, 97, 98]), thus too thin to support the rotator phase mechanism, at least in the experimental set up pioneered by Guttman *et al.* [38, 84, 85, 90]. By contrast, the elastic buckling mechanism fails to reproduce the observed size dependence of the sphere-icosahedron-platelet transition. Denkov *et al.* noted that while lowering the temperature, the smaller the droplet, the more the shape changes before reaching the bulk oil freezing point, with the largest droplets remaining spherical [37, 91]. Consistently, by imaging several individual droplets upon slow cooling, Guttman *et al.* reported quantitatively that small droplets undergo faceting at higher temperatures compared to large droplets (see micrograph in Fig. 4.2a and the experimental data in Fig. 4.4b, taken from Ref. [38], with slightly improved statistics). This cannot be explained either via the classic virus buckling picture, whose size-dependence is in fact opposite to that observed in icosahedral droplets [75], nor by postulating a similar interplay between

defect-driven stretching elasticity and surface tension. As both the stretching and the surface energy scale like R^2, the latter implies that, depending on the ratio between Y and the surface tension γ, at a given temperature, droplets are either always spherical (for small Y/γ values) or always icosahedral (for large Y/γ values), regardless of their size. Furthermore, in order for the elastic buckling mechanism to account for the icosahedra-platelets transition, one must assume $k \approx 10^{-1}\, k_B T$ [95], orders of magnitude smaller than the value $10^3\, k_B T$ estimated in Ref. [38].

We resolve this dilemma by demonstrating that elastic buckling can, in fact, explain not only the sphere-icosahedron-platelet transition, but also the size dependence observed in experiments, provided it is augmented with the following mechanisms: the spontaneous curvature of the frozen alkane-surfactant monolayer and gravity.

4.2 The model

4.2.1 Mechanical energy of deforming emulsion droplets

The starting point of our approach is the following functional describing the energy of a droplet of volume V and density ρ_{oil} enclosed by a crystalline monolayer and suspended in water, namely:

$$E = \frac{1}{2}\int \mathrm{d}A\, \left[2\gamma_0 + 4k(H - H_0)^2 + Y\sigma^2 + g\Delta\rho\, z^2 N_z\right] \,, \tag{4.1}$$

where $\sigma = \sigma_i^i/Y$ is the trace of the covariant stress tensor σ_{ij} arising in the interface in response to stretching deformations, H is the droplet mean curvature taking $H > 0$ for a sphere, H_0 the spontaneous curvature, g the gravitational acceleration, $\Delta\rho = \rho_{\text{water}} - \rho_{\text{oil}}$ the oil-water density difference and N_z the projection of the surface normal vector along the $z-$direction. The first term in Eq. (4.1) corresponds to the standard surface energy. The second term describes the energetic cost of bending, in terms of the departure of the droplet mean curvature from its preferential value H_0. The latter arises in droplets as a consequence of the asymmetry of the adsorbed surfactant molecules [99], and can be interpreted as a renormalization of the surface tension, analogous to that caused by an inhomogeneous Tolman length [100]:

$$\gamma' = \gamma - 4kH_0H \,, \tag{4.2}$$

where $\gamma = \gamma_0 + 2kH_0^2$ is the uniform part of the effective surface tension, inclusive of the contribution arising from the spontaneous curvature H_0. As we detail further below, this renormalization is instrumental to the observed size dependence. Since surface tension is the main restoring mechanism in spherical droplets, Eq. (4.2) implies that for $H_0 > 0$, the smaller the droplet the less it is prone to return to a spherical shape once it is deformed. The third term accounts for the in-plane stretching originating from the combined effect of the Gaussian curvature and the topological defects. Finally, the last term in Eq. (4.1) describes the gravity-buoyancy balance caused by the density difference $\Delta\rho$, here expressed as a surface integral by means of the divergence theorem.

In the following, we assume that all the material parameters are uniform across the surface and we search for the lowest energy configuration of the droplet as a function of γ and for various k, H_0, Y, and $g\Delta\rho$ values. Consistently with experimental studies, $\gamma \sim T$ is the only material parameter strongly affected by temperature within the experimental range and can, therefore, be used as a proxy for temperature [85, 94] (see also Appendix C). We compute the energy associated with three configurations depicted in Fig. 4.1a by modeling surfaces via triangulated meshes with rounded vertices and edges, specifically those shown in Fig. 4.7. The platelet, in particular, has a height-to-width ratio of around 1/10 at the center, consistently with three-dimensional electron microscopy reconstructions [101] (see also Fig. 4.6). Further details on the discretized surfaces are included in Appendix A.

4.2.2 Dimensionless energy and independent parameters

Measuring energy in units of k and length in units of $1/H_0$, we numerically calculate the dimensionless energy $\mathcal{E} = E/k$ for each surface as a function of the dimensionless size $r = H_0 R$, with $R = [V/(4\pi/3)]^{1/3}$. Namely:

$$\mathcal{E} = \mathcal{E}_W - \mathcal{E}_H r + (\Gamma \mathcal{E}_C + \Upsilon \mathcal{E}_S) r^2 + \Pi \mathcal{E}_G r^4 \,, \tag{4.3}$$

where the terms on the right-hand side denote the dimensionless form of the bending ($\mathcal{E}_W$, $\mathcal{E}_H$), capillary ($\mathcal{E}_C$), stretching ($\mathcal{E}_S$) and gravitational ($\mathcal{E}_G$) energies, obtained from the numerical integration of the mechanical energy Eq. (4.1) on a triangular discretization of the surface for each of the three droplet shapes studied. The various contributions are normalized as follows:

$$\mathcal{E}_W = 2 \int dA \; H^2 \,, \tag{4.4a}$$

$$\mathcal{E}_H R = 4 \int dA \; H \,, \tag{4.4b}$$

$$\mathcal{E}_S R^2 = \frac{1}{2} \int dA \; \sigma^2 \,, \tag{4.4c}$$

$$\mathcal{E}_C R^2 = \int dA \,, \tag{4.4d}$$

$$\mathcal{E}_G R^4 = \frac{1}{2} \int dA \; z^2 \, N_z \,. \tag{4.4e}$$

The bending energy has been split into the so called Willmore functional, $\mathcal{E}_W$, and the contribution associated with the spontaneous curvature, $\mathcal{E}_H R$. The numbers

$$\Upsilon = \frac{Y}{k H_0^2} \,, \qquad \Gamma = \frac{\gamma}{k H_0^2} \,, \qquad \Pi = \frac{g\Delta\rho}{k H_0^4} \,, \tag{4.5}$$

quantify the energetic cost of stretching, capillarity and gravity in comparison to bending, and they constitute the set of independent material parameters of the system.

With the exception of $\mathcal{E}_S$, all energy contributions depend exclusively on the shape of the droplet and can be straightforwardly computed using our meshes (Table 4.1).

The local curvatures are computed using the numerical methods described in Section 2.3. Details about the calculation of the stretching energy are further discussed below and in Appendix B.

4.2.3 Defect stress and stretching energy

In order to calculate the stretching energy in Eq. (4.4c), one needs to determine the local stress induced by the non-vanishing curvature of the droplet and by the topological defects populating the interfacial monolayer, by solving the Poisson equation

$$\nabla^2\sigma = \eta - K\,, \tag{4.6}$$

where ∇^2 is the Laplace-Beltrami operator, K the surface Gaussian curvature and η is the topological charge density of the defect distribution [72]. On a sphere, the latter consists of twelve topologically required, fivefold disclinations, positioned at the vertices of an inscribed icosahedron due to elastic interactions. Each disclination is surrounded by a "cloud" of topologically neutral dislocations, which ease the elastic distortion introduced in the lattice, thereby reducing the elastic energy [30, 52].

Following our work in Chapter 3, we express η in terms of a discrete set of "seed" disclinations, coupled with a continuous distribution of screening dislocations[2]. In particular, we consider:

$$\eta = \sum_{\alpha=1}^{\mathcal{V}} \left(\frac{\pi}{3}\, q_\alpha - \Phi\right) \delta(\boldsymbol{r} - \boldsymbol{r}_\alpha) + \frac{\Phi}{\mathcal{F}/\mathcal{V}} \sum_{\beta=1}^{\mathcal{F}} \delta(\boldsymbol{r} - \boldsymbol{r}_\beta)\,, \tag{4.7}$$

where $\mathcal{V}$ and $\mathcal{F}$ represent, respectively, the number of vertices and faces of the polyhedral droplets, $q_\alpha = 6 - z_\alpha$ is the topological charge of a $z_\alpha-$fold disclination located at position $\boldsymbol{r}_\alpha$ and Φ is the in-plane flux of the screening dislocation scars, originating in proximity of the vertices and terminating at positions $\boldsymbol{r}_\beta$ in the bulk of the faces of the polyhedral droplets, where $K \approx 0$ (see Fig. 4.7). This construction guarantees that $\int \mathrm{d}A\, \eta = 4\pi$ such that, consistently with the divergence and the Gauss-Bonnet theorems, both sides of the stress equation vanish upon integration over the entire surface. While faceting keeps the symmetry of the twelve $q_\alpha = 1$ disclinations in the icosahedron, flattening brings pairs of disclinations close together, essentially leading to merging of defects [95]. We consider six $q_\alpha = 2$ disclinations in the case of the hexagonal platelet, located at mid height close to the vertices of the hexagonal projection. Fig. 4.7 shows the modelled configurations for each geometry.

The optimal dislocation flux Φ for a given surface is found by minimizing the energy $\mathcal{E}_S$ [102], resulting in Eq. (4.9). We note however that all our results still hold qualitatively under the assumption of little to no screening (i.e. $\Phi = 0$) (see also Appendix B). The stress field generated in each shape by the corresponding defect density in Eq. (4.7) is plotted in Fig. 4.3.

[2]Specifically, in Appendix A.3 in the previous chapter, we discuss how the defect charge density in our framework is generalized in a simple way for other geometries and different defect distribution in the lattice. Applying Eq. (3.31) to the hexagonal platelet is then straightforward.

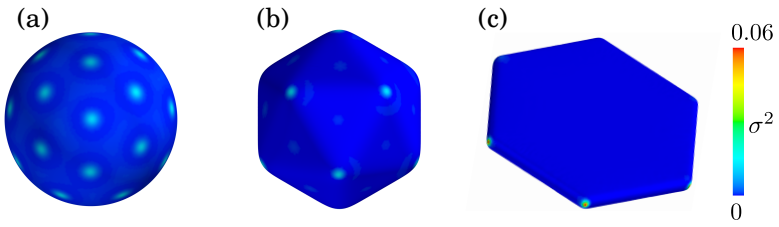

Figure 4.3: Calculation of the defect-induced stress field at the interface of the droplets Defect-induced stress field σ^2 on the crystalline interface with screening dislocations, computed from the charge density η in Eq. (4.7).

Energy	Sphere	Icosahedron	Platelet
$\mathcal{E}_W$	25.4	49.2	209.6
$\mathcal{E}_H$	50.3	55.9	112.0
$\mathcal{E}_C$	12.6	12.9	34.6
$\mathcal{E}_S$	0.0028	0.0013	0.0016
$\mathcal{E}_G$	4.19	4.00	0.555

Table 4.1: Contributions to the dimensionless energy Eq. (4.3) for the spherical, icosahedral and hexagonal droplets, calculated using Eqs. 4.4.

4.3 Results

Within this framework, we have numerically calculated and compared the energies $\mathcal{E}_{\text{sph}}$, $\mathcal{E}_{\text{ico}}$ and $\mathcal{E}_{\text{pla}}$ of the spherical, icosahedral and platelet conformations. The outcome of our analysis is summarized in Table 4.1 and in the phase diagram of Fig. 4.4.

4.3.1 Faceting transition

First, we focus on the faceting transition (i.e. sphere-icosahedron), for which buoyancy plays a marginal role (see $\mathcal{E}_G$ in Table 4.1) and thus can be temporarily neglected. In this case, the total energy is just a quadratic function of the dimensionless size r, from which the corresponding phase boundaries can be easily computed as shown by the dashed lines in Fig. 4.4a. The defect configuration that minimizes the stretching energy $\mathcal{E}_S$ consists of twelve fivefold disclinations (i.e. $q_\alpha = 1$) approximately located at the vertices of an icosahedron and surrounded by screening dislocations, so that $\eta \approx K$ in their vicinity. In the absence of restoring mechanisms favoring spherical shapes, as bending and capillarity, icosahedral shapes would be preferred over spherical ones, for *any* temperature and droplet size. Since the icosahedron has a larger area and bending energy compared to a sphere of the same volume (both $\mathcal{E}_W$ and $\mathcal{E}_H$ diverge for a perfectly sharp icosahedron), these restoring mechanisms render the icosahedral conformation energetically optimal only at low temperature, where capillarity is sufficiently weak (i.e. the yellow region of panel a in Fig. 4.4). Furthermore, as surface tension becomes effectively smaller for decreasing droplet size

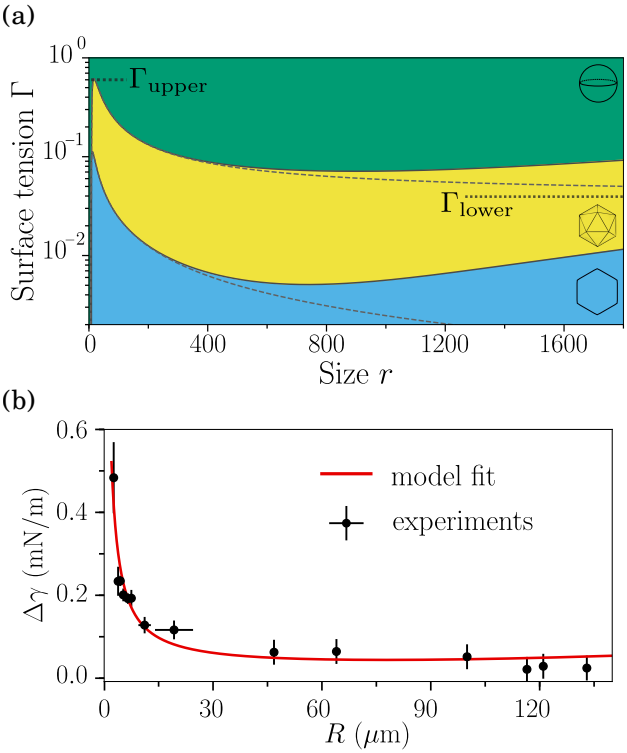

Figure 4.4: Phase diagram of the faceting and flattening of droplets (a) Morphological phase diagram in the $(r, \Gamma)-$plane obtained by comparing the energies of spherical, icosahedral and platelet-shaped droplets calculated via Eq. (4.3). The bound values of Γ for faceting, Eq. (4.8), are indicated with dotted lines. The dashed lines correspond to the phase boundaries when buoyancy effects are ignored, while the solid ones are for $\Pi = 10^{-8}$. In this diagram, we use $\Upsilon = 4$. (b) Experimental estimate and theoretical fit of the difference between the surface tension at the sphere-icosahedron and icosahedron-platelet transitions, $\Delta\gamma = \gamma_{\text{sph}-\text{ico}} - \gamma_{\text{ico}-\text{pla}}$, as a function of droplet radius [38]. The values of Υ and Π used to create (a) follow from the fitted model curve shown here. See Appendix C for details.

due to the spontaneous curvature (see Eq. (4.2)), smaller droplets generally undergo the faceting transition at higher temperature than large droplets, consistently with the experimental observations (Fig. 4.2a and Ref. [38]).

At a fixed Γ value, the critical size at which the transition takes place is found by solving the equation $\mathcal{E}_{\text{ico}} = \mathcal{E}_{\text{sph}}$ with respect to $r > 0$. These solutions yield the range of parameters in which spherical and icosahedral droplets coexist, namely:

$$0 < \Gamma + \Upsilon \frac{\Delta\mathcal{E}_S}{\Delta\mathcal{E}_C} < \frac{\Delta\mathcal{E}_H^2}{4\Delta\mathcal{E}_W\Delta\mathcal{E}_C} , \tag{4.8}$$

where $\Delta\mathcal{E}_i$ $(i = S, C, H, W)$ labels the various contribution of the $\mathcal{E}_{\text{ico}} - \mathcal{E}_{\text{sph}}$ energy difference. The upper bound of this inequality, Γ_{upper} corresponds to the peak of the yellow region in Fig. 4.4a, above which capillarity dominates and droplets are always

spherical regardless of their size. The abscissa of the peak of the sphere-icosahedron phase boundary, $r = 2\Delta\mathcal{E}_W/\Delta\mathcal{E}_H$, approximates the minimal droplet radius $r_{\min}$ at which icosahedral droplets can be found. For $r < r_{\min}$, the Gaussian curvature of the sphere is sufficiently large to accommodate the angular deficit introduced by the fivefold disclinations and faceting does not occur, except in the limit of vanishing bending rigidity. The lower limit $\Gamma_{\text{lower}} = -\Upsilon\Delta\mathcal{E}_S/\Delta\mathcal{E}_C$ in Eq. (4.8), defines a lower critical surface tension, indicated in Fig. 4.4, below which all droplets of size $r > r_{\min}$ are icosahedral.

We now look at the effect of buoyancy in the faceting transition, which only affects the large$-r$ region of the phase diagram by favoring icosahedra over spheres (see also Table 4.2 —color boundary in Fig. 4.4a). In general, the gravitational energy can be lowered by reducing the distance between the droplet center of mass and the top wall of the sample container. In particular, for regular polyhedra with D_{nh} and D_{nd} point group, $\mathcal{E}_G R = (4\pi/3)\, h/2$ with h the height of the droplet, and this can be achieved by aligning one of the flat faces orthogonally to the $z-$direction. As $h/2 < R$ in the faceted droplets of conserved volume, buoyancy widens the icosahedral phase at large r values.

4.3.2 Flattening transition

Next we focus on the flattening transition (i.e. icosahedron-platelet). Experimentally, this is observed at ultra-low (or even transiently negative) values of the surface tension [85]. In this regime, the system lacks of the main restoring mechanism favoring spherical shapes and the icosahedral configuration represents the absolute minimum of the elasto-capillary energy for large Υ values. As the area of a platelet is larger than that of an icosahedron with the same volume, in the absence of spontaneous curvature and/or gravitational effects, the droplet flattening can only occur at negative Γ values. A positive spontaneous curvature, by contrast, favors platelets over icosahedra at small r values as a consequence of the larger mean curvature at the edges and vertices.

Furthermore, upon orienting orthogonally with respect to the $z-$direction, platelets can raise their center of mass to reduce their gravitational energy to arbitrarily small values, at the cost of increasing the stretching energy by pairwise merging the twelve fivefold disclinations into six fourfold disclinations (i.e. with charge $q_\alpha = 2$). This causes icosahedral droplets to morph into hexagonal platelets, where the Gaussian curvature at the vertices is sufficiently large to compensate for the elastic distortion introduced by the higher topological charge, resulting in a modest increase of the stretching energy (see Table 4.1). Because of spontaneous curvature at smaller scales and buoyancy at larger ones, flattening is possible at low but still positive surface tension values (see Fig. 4.4), consistently with experimental observations.

4.3.3 Energy contributions at different scales

In Table 4.2, we report the magnitude of the dimensionless energy differences, $\Delta\mathcal{E} = \mathcal{E}_{\text{ico}} - \mathcal{E}_{\text{sph}} = 0$, which determines the faceting phase boundary in Fig. 4.4a, at different size scales. We fix $\Gamma = 0.1$. Since each energy term scales differently with r, their

relative magnitude varies with the droplet size. At the smallest sizes, it is the bending term, including the spontaneous curvature, which plays a leading role in the observed size-dependent behavior of the faceting. For droplets of $r \approx 500$, we find that elasticity competes with the surface tension, while buoyancy is the main deforming component at the large scale.

r	$\lvert\Delta\mathcal{E}_W\rvert$	$\lvert\Delta\mathcal{E}_H\rvert\ r$	$\lvert\Gamma\Delta\mathcal{E}_C + \Upsilon\Delta\mathcal{E}_S\rvert\ r^2$	$\Pi\lvert\Delta\mathcal{E}_G\rvert\ r^4$	Leading term
$\approx 5 \times 10$	24	300	60	0.01	Bending
$\approx 5 \times 10^2$	24	3000	6000	100	Stretching
$\approx 5 \times 10^3$	24	3×10^4	6×10^5	10^6	Gravitational

Table 4.2: Estimate of the energy contributions at different scales during faceting. The transition is determined by the difference in the dimensionless energy, Eq. (4.3), between a spherical droplet and an icosahedral one, $\Delta\mathcal{E} = \mathcal{E}_{\text{ico}} - \mathcal{E}_{\text{sph}}$. The dimensionless material parameters here are taken as $\Gamma = 0.1$, $\Upsilon = 4$ and $\Pi = 10^{-8}$.

A similar analysis holds for the flattening at $\Gamma = 0.01$, where one expects large icosahedral droplets and small platelets (see Fig. 4.4). In this second transition, the stronger influence of gravity is reflected quantitatively in a larger $\Delta\mathcal{E}_G$.

4.3.4 Model fit to experimental data

To assess the significance of our predictions, we have fitted the difference $\Delta\gamma = \gamma_{\text{sph-ico}} - \gamma_{\text{ico-pla}}$ between the surface tension at the sphere-icosahedron and icosahedron-platelet transitions as a function of the droplet radius, to the experimental data shown in Fig. 4.4b. The black markers correspond to averaged measurements of droplets of different initial size, which are imaged as they undergo faceting and flattening (see Ref [38] and Appendix C for further explanation). Using the dimensionless energy contributions for every shape in Table 4.1, from the expression for the total energy we calculate the phase boundaries for each transition as a function of size, in terms of the material constants k, H_0, Y and $\Delta\rho$ (see Eq. (4.10). Upon fixing $\Delta\rho = 0.25\,\text{g/cm}^3$ [90, 95] and $k = 10^3\,k_BT$ [38], we fit the model $\Delta\gamma(R)$ and obtain $Y \approx 4.4\,\text{mN/m}$ and $H_0^{-1} \approx 58\,\text{nm}$, consistently with current knowledge (see Appendix C for details). The fit is shown as the red curve shown in Fig. 4.4b.

The dimensionless parameters used in the morphological phase diagram in Fig. 4.4a correspond to the fitted material constants. In particular, we adopt $\Upsilon = 4$ and $\Pi \approx 10^{-8}$. Note that a small variation in γ, such as those reported in Ref. [90], would not change the results, provided that the dimensionless values of Υ, Γ and Π are kept the same, which can be achieved by a small variation of k, H_0 and Y.

4.3.5 Predictions for different material parameters

We look at the effect of the mechanical properties of the frozen interfacial monolayer, embodied in the number Υ, for both transitions. Assuming Γ fixed, we solve the equations $\mathcal{E}_{\text{sph}} = \mathcal{E}_{\text{ico}}$ and $\mathcal{E}_{\text{ico}} = \mathcal{E}_{\text{pla}}$ with respect to the r and Υ in the proximity of the sphere-icosahedron and icosahedron-platelet phase boundaries. The corresponding

solutions are displayed in Fig. 4.5 for $\Gamma = 0.33$ and $\Gamma = 0.056$. These are intermediate values from the range in Eq. (4.8) when $\Upsilon = 4$, where we observe the coexistence of different shapes for differently sized droplets, as in experiments.

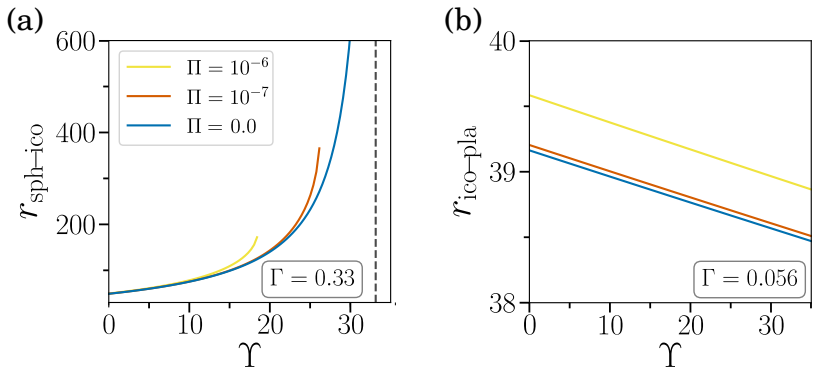

Figure 4.5: Shape transitions for other values of material parameters. Critical size for the faceting (a) and flattening (b) transitions, obtained by solving the equations $\mathcal{E}_{\mathrm{sph}} = \mathcal{E}_{\mathrm{ico}}$ and $\mathcal{E}_{\mathrm{ico}} = \mathcal{E}_{\mathrm{pla}}$ with respect to r, versus the Υ parameter. Note in (a) that for each Π, there is a maximal Υ beyond which no critical radius exist for faceting, as all droplets are icosahedral.

In the case of the faceting transition, an increase in Υ corresponds to a shift of the phase boundary to higher values of surface tension due to the lower stretching energy of icosahedral droplets. Therefore, at a given Γ, the critical droplet size associated with the faceting transition increases with Υ, until a limiting value where all droplets are icosahedral at any $r > r_{\mathrm{min}}$. For $\Pi = 0$, this value corresponds to the dashed vertical line in Fig. 4.5a. By contrast, the critical radius associated with the flattening transition (Fig. 4.5b) is a slowly decreasing function of Υ, due to the higher stretching in the platelet. It is only at smaller sizes, where bending dominates (see Table 4.2), that the curvature gain in the platelet is enough to compensate for this slight energy increase. Decreasing Υ, however, narrows the gap between the faceting and flattening transition by reducing the range of the icosahedral phase. As $\Upsilon \to 0$, the two critical radii are comparable in magnitude, and the temperature range at which spheres coexist with platelets is widened.

Finally, both critical radii increase under the effect of gravity, as this facilitates departure from isotropic shapes. Also a consequence of this, the limiting Υ value where droplets of all sizes are icosahedral, decreases for increasing Π values, as seen in panel (a) of Fig. 4.5.

4.4 Conclusions

We theoretically addressed the mechanical origin of the faceting and flattening transitions that, starting from the pioneering work of Denkov [37] and Guttman *et al.* [38] have been systematically reported in emulsion droplets stabilized by a frozen layer of

alkane molecules and surfactants. Using a combination of continuum mechanics and three-dimensional computer modeling, we demonstrated that both transitions originate from the fourfold interplay between defect-driven stretching, bending elasticity, capillarity and gravity.

Because of the scaling behavior of various energy contributions, the shape deformations are influenced by the initial volume of the spherical droplets. In particular, we highlighted the importance of the positive spontaneous curvature of the interface monolayer for small droplets, that, by effectively hindering the magnitude of capillary forces, allows one to reproduce the counterintuitive size-dependence observed in the experiments. At intermediate sizes, the faceting of spherical droplets into icosahedral shapes is strongly driven by the elasticity of the interfacially-frozen monolayer, acting against the area-minimizing capillary forces. The buckling of the interface screens the stress introduce by the twelve fivefold topological disclinations. The flattening of icosahedral droplets into platelets causes pairs of defects to come into closer contact, for which the increase of stress is further screened by a higher curvature in the vicinity of the hexagonal vertices. Buoyancy however drives the flattening in larger droplets. We showed that both the icosahedral droplets and the hexagonal platelets progressively reduce their gravitational energy, upon orientation of one of the flat faces orthogonally to the direction of gravity, precisely as observed in experimental micrographs.

Additionally, we quantitatively compare the results from our mechanical model against experimental measurements of the faceting and flattening surface tension for droplets across a wide range of sizes, to which we find a remarkable agreement. We showed that the same qualitative phase behavior holds for emulsion systems with different material properties, generally resulting in differences in the critical temperature and the critical size at which faceting and flattening occur.

In short, our model shows that the faceting of emulsion droplets with an interfacially-frozen monolayer against capillary forces is governed by the spontaneous curvature of the interface and defect-elasticity. The consequential flattening of the icosahedral droplets into hexagonal platelets, despite the large area increase, is allowed at positive values of surface tension due to buoyancy and spontaneous curvature. While more advanced theoretical models may be needed to describe the behavior of multicomponent droplets [93], our present work provides the basis for these more complex future models.

Acknowledgements

We thank Pierre Haas, Ray Goldstein and Moshe Deutsch for illuminating discussions and Shir R. Liber and Alexander V. Butenko for technical assistance. This work is partially supported by Netherlands Organisation for Scientific Research (NWO/OCW), as part of the D-ITP program, the Vidi scheme, the Frontiers of Nanoscience program, and the Israel Science Foundation, grant no. 1779/17.

4.5 Appendices

Appendix A Droplet geometries

All triangulated surfaces were constructed using the software Surface Evolver [87]. The rounded icosahedron was obtained starting from the sharp one with perfectly flat faces, which were refined to have around 2×10^4 mesh points. Using the software, we allowed an area-minimizing relaxation of the icosahedron into a sphere. The icosahedral shape used for this study is an intermediate stage of the relaxation with rounded edges and vertices of finite curvature, while the sphere is the final shape (see B.1 in Chapter 3 for more details). Similarly, the hexagonal platelet was initialized as a perfectly sharp polyhedron with $\approx 2 \times 10^4$ mesh points and its edges and vertices were rounded with a smoother relaxation and further regularization. The rounded edges of the icosahedron and the platelet have on average an approximate mean curvature of $\bar{H}^2_{\text{ico}} R^2 = 3.2$ and $\bar{H}^2_{\text{pla}} R^2 = 21.9$ respectively, in contrast to that of the sphere $\bar{H}^2_{\text{sp}} R^2 = 1$.

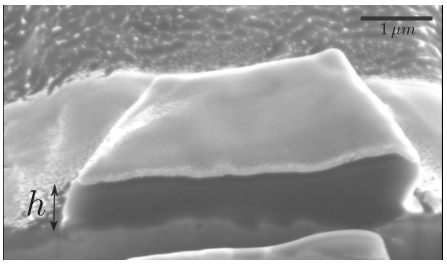

Figure 4.6: Geometry of a flattened droplet. Focused Ion Beam (FIB) slicing through a polymerized hexagonal platelet, evincing the approximate height-to-width ratio in these droplets to be of the order of 1 : 10. Taken and modified with permission from the Supplementary Information in Ref. [101].

The height of the resulting platelet, measured along the direction of gravity is 7% the width of the hexagonal face, consistent with scanning electron microscopy of these droplets [101]. See for example in Fig. 4.6 a 3D cross-section of a hexagonal platelet.

Appendix B Defect stress and stretching energy

As outlined in the main text, the stretching energy $E_S = Y/2 \int dA\, \sigma^2$, where Y is the Young's modulus, requires finding the stress field σ by solving the equation

$$\nabla^2 \sigma = \eta - K\,, \qquad \text{(4.6 revisited)}$$

where ∇^2 is the Laplace-Beltrami operator, K is the Gaussian curvature and η is the topological charge density of the defects, and it therefore depends on the specific lattice structure of the frozen interface of the droplets. More specifically, it depends on the number, charge and position of the lattice defects.

Given the nanoscopic nature of the surfactant-alkane structure at the interface, and the microscopic scale of the droplets themselves, the crystalline monolayer is expected to have a high density of lattice sites. We therefore take the continuous approach described in Chapter 3 for dense crystals, which takes into account possible screening of dislocation structures in the vicinity of the topological disclinations.

Within this framework, η can be expressed in terms of the topological charge density of twelve topologically required disclinations plus the effective charge density resulting from a continuous distribution of screening dislocations, i.e. Eq. (4.7) in the main text. The latter is described by two sets of discrete defects with different charge: defects screening out the disclination-induced stress in the vicinity of the disclination positions $\boldsymbol{r}_\alpha$, and additional defects located close to the far end of these dislocation structures, in positions $\boldsymbol{r}_\beta$.

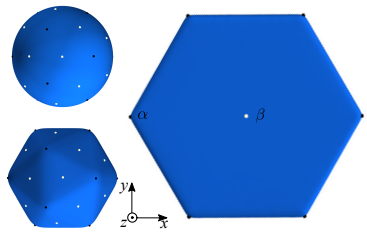

Figure 4.7: Modeled droplet shapes for the calculation of the energy. These are to scale according to a fixed size R, and here viewed along the direction of gravity. Each surface is marked with the positions of the "seed" disclinations $\boldsymbol{r}_\alpha$ (black) and the terminating positions of the dislocation flux $\boldsymbol{r}_\beta$ (white) assumed in the calculation of Eq. (4.7). The markers have been magnified and do not reflect the underlying discretization of the surface.

As explained in section 3.3 in Chapter 3,the resulting stretching energy is found to have a quadratic scaling with the droplet size and can be expressed as

$$E_S = Y\mathcal{E}_S R^2 = \frac{Y}{2}\left[c_0 - \frac{c_1^2}{4c_2}\right] R^2\,, \tag{4.9}$$

where c_0, c_1 and c_2 are called the geometric coefficients, as depend on the particular surface geometry and the distribution of defects for the charge density η in Eq. (4.7). For more details on this calculation we refer the reader to the work leading to Eq. (3.15). In particular, we use here the coefficients calculated in this chapter for the sphere and the rounded icosahedron (see Table 3.1). In the case of the platelet, we calculate the coefficients for a lattice having six seed disclinations with charge $q_\alpha = 2$ located at mid height by the hexagonal vertices and two scar sinks at the center of each hexagonal faces, as seen in Fig. 4.7. We show the resulting geometric coefficients for all three droplet geometries in Table 4.3. Finally, we note that in the case of little to no screening, $\Phi = 0$ in Eq. (4.7), the coefficients $c_1 = 0$ and c_2=0, therefore equivalent to a rescaling of the coupling parameter Y (and hence Γ), which is different for every shape.

Appendix C Experimental validation

The experimental data shown in Fig. 4.4b of the main text were taken with permission from Fig. S4 in Ref. [38], used in this work with slightly improved statistics (see text Ref. [38] for more details). In these experiments, droplets of various initial sizes are imaged at slow cooling, in order to identify the temperatures at which the individual

Shape	c_0	c_1	c_2
Sphere	0.046	-0.12	0.093
Icosahedron	0.0061	-0.039	0.11
Platelet	0.0032	-0.042	8.2

Table 4.3: Coefficients of the stretching energy, Eq. (4.9), for the spherical, icosahedral and hexagonal geometries, calculated using the framework described in Chapter 3.

droplets first facet and further flatten, and use these to measure the surface tension then. Given the scatter in the measurements for different droplets, it is convenient to take the difference between the surface tension at the sphere-icosahedron transition $\gamma_{\mathrm{sph-ico}}$ and the icosahedron-platelet transition $\gamma_{\mathrm{ico-pla}}$, denoted as $\Delta\gamma(R)$, where R is the radius of the spherical droplet before faceting. We consider the results for droplets of sizes in the range $R = 2.2 - 133\,\mu$m, and further bin these data to reduce dispersion.

The value of the surface tension γ is estimated under the assumption that this is the only material parameter significantly affected by temperature within the experimental range [38]. This is justified by the fact that the bulk modulus is related, through the Grüneisen constant, to the heat capacity and the thermal expansion [103]. The thermal expansion for similar interfacial crystals was measured to be temperature-independent in the relevant range of temperatures [51]. Moreover, since dS/dT of the interfacial crystal is constant, up to its melting point [90], the temperature-variation of the heat capacity $C = T(dS/dT)$ should be $\sim 0.3\%/^{\circ}C$. Thus, the bulk modulus does not significantly change in the relevant range of temperatures. Similar arguments allow the assumed temperature-independence of the other moduli to be justified [104].

We obtain the model prediction for $\Delta\gamma(R)$ starting from the energy functional proposed in Eq. (4.3) of the main text. Using the dimensionless energy terms introduced in Eq. (4.4) and whose values are be found in Table 4.1 for the three shapes studied, we can write the energy as

$$E = k\mathcal{E}_W - kH_0\mathcal{E}_H R + (\gamma\mathcal{E}_C + Y\mathcal{E}_S)R^2 + g\Delta\rho\mathcal{E}_G R^4\,, \tag{4.10}$$

in terms of the material constants k, γ, Y, and the density difference between the oil and water. We solve the equations $E_{\mathrm{sph}} = E_{\mathrm{ico}}$ and $E_{\mathrm{ico}} = E_{\mathrm{pla}}$ to find the critical surface tension as a function of size $\gamma(R)$, at the faceting and the flattening respectively. We can then compare the experimental measurements to the model prediction for $\Delta\gamma = \gamma_{\mathrm{sph-ico}} - \gamma_{\mathrm{ico-pla}}$. Taking $\Delta\rho = 0.25\,\mathrm{g/cm^3}$ [90, 95] and $\kappa = 10^3 k_B T$ [38], we fit $\Delta\gamma(R)$ to the experimental measurements, considering Y and H_0 as free fitting parameters. Using non-linear least squares fitting, we find the solid red curve shown in Fig. 4.4b, for which $H_0^{-1} \approx 58\,$nm, and $Y \approx 4.4\,$mN/m. For an interface of thickness 2 nm [38], this roughly corresponds to a 3D Young's modulus of $Y_{3\mathrm{D}} = 2\,$MPa. Using the material constants above, we get an estimate for the dimensionless model parameters. In particular, Eq. (4.5) results in $\Upsilon = 4$ and $\Pi \approx 10^{-8}$, which we take to construct the phase diagram in Fig. 4.4a. The effect of varying these values is discussed in Section 4.3.5.